






Exploring the Nature of EUV Waves in a Radiative Magnetohydrodynamic Simulation

Can Wang^{1,2} , Feng Chen^{1,2} , and Mingde Ding^{1,2} 

¹ School of Astronomy and Space Science, Nanjing University, Nanjing 210023, People's Republic of China; chenfeng@nju.edu.cn

² Key Laboratory for Modern Astronomy and Astrophysics (Nanjing University), Ministry of Education, Nanjing 210023, People's Republic of China

Received 2021 January 21; revised 2021 March 3; accepted 2021 March 17; published 2021 April 13

Abstract

Coronal extreme-ultraviolet (EUV) waves are large-scale disturbances propagating in the corona, whose physical nature and origin have been discussed for decades. We report the first three-dimensional (3D) radiative magnetohydrodynamic simulation of a coronal EUV wave and the accompanying quasi-periodic wave trains. The numerical experiment is conducted with the MURaM code and simulates the formation of solar active regions through magnetic flux emergence from the convection zone to the corona. The coronal EUV wave is driven by the eruption of a magnetic flux rope that also gives rise to a C-class flare. It propagates in a semicircular shape with an initial speed ranging from about 550 to 700 km s⁻¹, which corresponds to an average Mach number (relative to fast magnetoacoustic waves) of about 1.2. Furthermore, the abrupt increase of the plasma density, pressure, and tangential magnetic field at the wave front confirms fast-mode shock nature of the coronal EUV wave. Quasi-periodic wave trains with a period of about 30 s are found as multiple secondary wavefronts propagating behind the leading wave front and ahead of the erupting magnetic flux rope. We also note that the true wave front in the 3D space can be very inhomogeneous; however, the line-of-sight integration of EUV emission significantly smoothes the sharp structures in 3D and leads to a more diffuse wave front.

Unified Astronomy Thesaurus concepts: [Radiative magnetohydrodynamics \(2009\)](#); [Solar extreme ultraviolet emission \(1493\)](#); [Solar corona \(1483\)](#); [Solar coronal waves \(1995\)](#); [Solar activity \(1475\)](#)

Supporting material: animations

1. Introduction

Large-scale disturbances propagating in the corona, known as “EIT waves” or “EUV waves,” were first detected by Thompson et al. (1998) with the Extreme-ultraviolet Imaging Telescope (EIT) on the Solar and Heliospheric Observatory (SOHO). Upon discovery, they were suggested to be the coronal counterpart of Moreton waves, which are chromospheric disturbances associated with solar flares (Moreton 1960; Athay & Moreton 1961). This intriguing phenomenon was extensively studied in the following decades with observations by EIT and the Solar Terrestrial Relations Observatory that provide a multiperspective view. The coronal EUV waves propagate in a wide range of speed spanning from a few tens to a few hundreds of km s⁻¹ (Klassen et al. 2000; Robbrecht et al. 2001; Liu et al. 2011; Muhr et al. 2014) and exhibit various interactions with surrounding magnetic structures, for example, they can be refracted or reflected by the strong magnetic field, or transmit cross the topological boundary of solar active regions and coronal holes (Gopalswamy et al. 2009; Olmedo et al. 2012; Shen et al. 2013, 2019). The complex behaviors revealed by observations led to a hot debate on the physical nature of EUV waves, and a variety of theoretical models have been put forward. The interpretation of the EUV waves can be divided into three major categories: wave model (e.g., Uchida 1974; Warmuth et al. 2004; Wills-Davey et al. 2007) that considers EUV waves as fast magnetoacoustic waves or shocks, pseudo-wave model (e.g., Attrill et al. 2007; Delannée et al. 2008) that interprets the observed disturbance as a fact of reconfiguration of coronal magnetic field, and hybrid model (e.g., Chen et al. 2002, 2005) that comprises both wave and nonwave components. Comprehensive reviews on the observational properties and models of coronal EUV waves have been

given by Liu & Ofman (2014), Warmuth (2015), and Long et al. (2017).

In the past decade, the Atmospheric Imaging Assembly (AIA) on board the Solar Dynamics Observatory was allowed to acquire observational data with unprecedented high spatial and temporal resolutions, revealing more detailed features of EUV waves. Events with both wave and nonwave components are found to be very common (Chen & Wu 2011; Asai et al. 2012; Liu et al. 2013; Cunha-Silva et al. 2018; Fulara et al. 2019). Such observations are also supported by three-dimensional (3D) models (Cohen et al. 2009; Downs et al. 2012).

In spite of the continued improvement of observing techniques, the observational data have an obvious shortcoming that they cannot directly reveal the in situ physical parameters that are crucial to determine the nature of EUV waves. On the other hand, radiative magnetohydrodynamic (RMHD) simulations with sophisticated physical processes allow for a direct and quantitative comparison between model synthesized observables and real solar observations. Furthermore, although the physical processes considered in the simulation might not pose a significant direct impact on transient phenomena (such as coronal EUV waves), they play a crucial role in reproducing realistic thermodynamic properties of plasma, and this allows investigation of wave properties under conditions more similar to that of the real Sun. Recently, realistic RMHD simulations have been applied to the production of solar flares for the first time (Cheung et al. 2019) and have successfully reproduced key properties of real solar flares. We present in this Letter the analysis of the first realistic RMHD simulation of a solar flare that drives a coronal EUV wave, as well as the accompanying quasi-periodic wave trains. This provides us an exceptional data set to study the evolution of physical quantities beneath the observational properties of the coronal EUV wave.

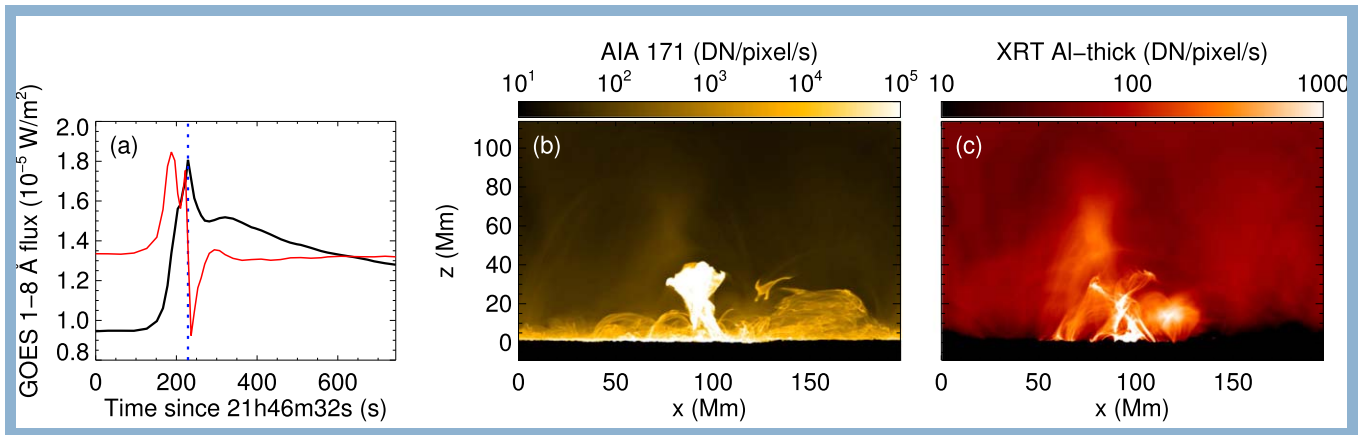


Figure 1. Overview of the flare event simulated by the MURaM code that triggers the coronal EUV wave. (a) Synthetic GOES-15 1–8 Å flux. The red line shows the temporal derivative of the GOES flux, which is considered as the indicator of the impulsive phase. The blue dotted line indicates the time instance of the image shown in (b) and (c). (b) Synthetic AIA 171 Å image at the flare peak ($t = 228$ s). The view point corresponds to observing an event that occurs at the solar limb. (c) Synthetic XRT Al-thick image at the same time and from the same view point as in (b). The animated version shows an evolution of 743.7 s.

(An animation of this figure is available.)

The rest of the Letter is organized as follows. Section 2 gives a brief description on the numerical simulation. We present in Section 3 the analysis on the morphology and kinematics of the wave and changes of physical quantities across the wave front. In the end, a discussion on the comparison between the simulated wave and observations is presented in Section 4.

2. Numerical Simulation

We analyze the data from a 3D RMHD simulation spanning from the uppermost convection zone to the corona. The simulation domain is 196.6 Mm wide in the horizontal directions. The vertical extent is 122.9 Mm, with the bottom boundary located at 9 Mm below the photosphere. The domain is resolved by 1024×1024 grid points in the horizontal direction and 1920 grid points in the vertical direction, yielding a spatial resolution of 192 and 64 km in the two directions, respectively. The simulation was conducted with the MURaM code (Vögler et al. 2005; Rempel 2017), which solves fully compressible MHD equations and implements a sophisticated treatment on the energy balance in the solar atmosphere. The latter is a crucial requirement for making a quantitative comparison between synthesized observables (e.g., AIA images) and real observations.

In this simulation, the magnetic flux bundles generated in a solar convective dynamo (Fan & Fang 2014) are introduced through the bottom boundary. These flux bundles emerge to the photosphere and create sunspots that can reproduce key properties of active regions on the real Sun (Chen et al. 2017). This simulation has a greatly expanded vertical domain that allows the magnetic flux to emerge further into the corona. In the full evolution of 48 hr, the complex and strong active regions formed by the emerging magnetic flux give rise to more than 50 flares in C class and 1 flare in M class. A comprehensive analysis on this simulation will be presented in a separate study.

In this Letter, we focus on a short time period of 743.7 s from $21^{\text{h}}46^{\text{m}}32^{\text{s}}$ (t_0), while the simulation is assumed to start from $00^{\text{h}}00^{\text{m}}00^{\text{s}}$ (hereafter, time is shown relative to t_0). During this time period, a flare occurs at $t \approx 200$ s and generates an evident coronal EUV wave. The synthetic GOES 1–8 Å flux in Figure 1(a) shows that in the impulsive phase the GOES flux is

steeply increased by about $8.5 \times 10^{-6} \text{ W m}^{-2}$ from the pre-flare level. The flare is produced by the eruption of a magnetic flux tube. Figures 1(b) and (c) display synthetic AIA 171 Å and XRT Al-thick images at the flare peak ($t = 228$ s) from a side view, respectively. The former presents the erupting flux rope, which eventually falls back to the solar surface, and the latter highlights hot plasma giving rise to soft X-ray emission.

3. Results

3.1. Morphology of the Coronal EUV Wave

The EUV wave can be clearly seen in the running difference of AIA images shown in Figure 2, and the full evolution of the wave is covered by the accompanying animation. The wave is ignited during the impulsive phase of the flare. In this phase, instead of a solitary wave front, many small ripples (pink arrow in Figure 2(a)) are generated at multiple locations surrounding the rising flux rope (blue arrow in Figure 2(a)). As these ripples propagate outward from the flare site, a large-scale leading wave front (yellow arrow in Figure 2(c)) is formed. The leading wave front appears to be a smooth semicircle and sweeps the entire domain. The eruption of the flux rope eventually stops near $z = 50$ Mm. However, it can be seen in the animation of Figure 2 that the flux rope continues to trigger small ripples that propagate outward. When the apex of the leading wave front reaches the top of the domain, several weaker wavefronts are formed within the bright leading wave front and ahead of the flux rope. These wavefronts appear to be very similar to the quasi-periodic wave trains (green arrows in Figure 2(c)) found by Liu et al. (2012). The top boundary of the domain allows outflows but is not perfectly nonreflective; thus, after $t = 324$ s when the apex of the leading wave front reaches the top of the domain, a reflection can be observed. The evolution afterward no longer represents the situation on the real Sun, and hence is excluded from the quantitative analysis. Nonetheless, the reflection suggests that the EUV wave retains sufficient kinetic energy to propagate farther if not confined by the simulation boundary.

The simulation also provides the opportunity to analyze the wave in the 3D space. For this purpose, we visualize the wave front by the running difference of electron number density

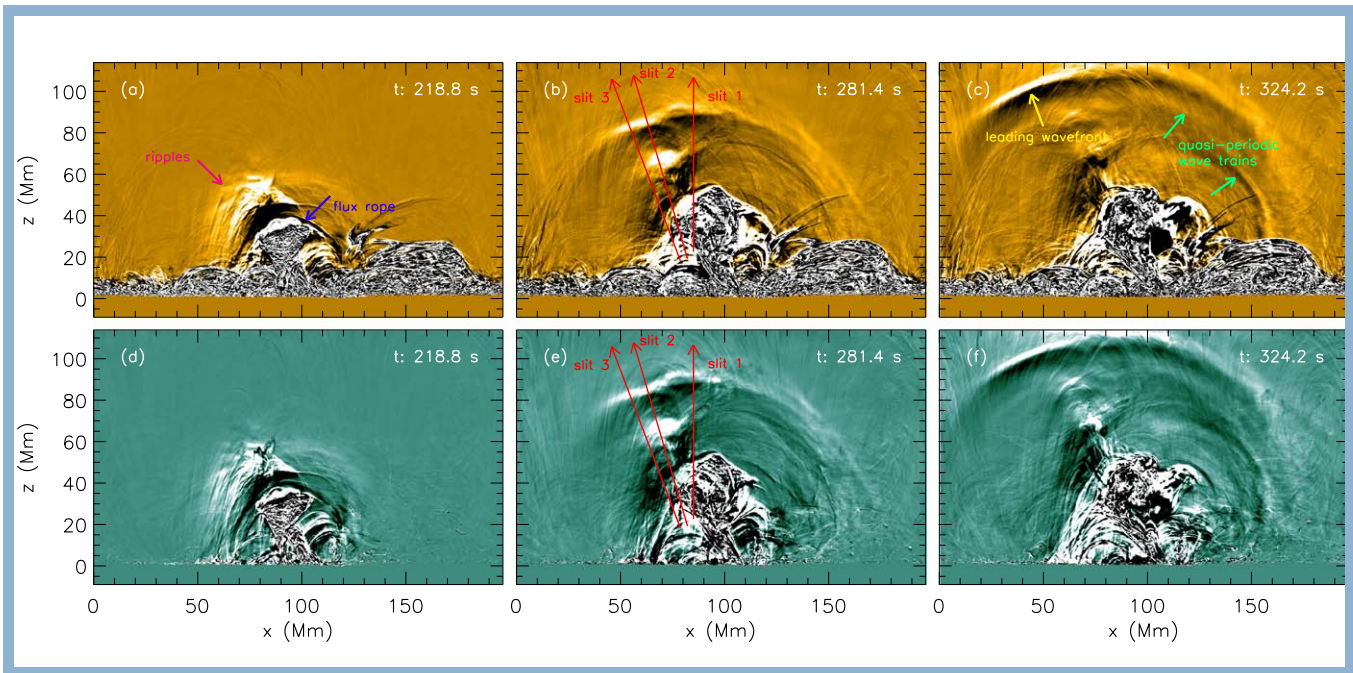


Figure 2. Running difference of the synthetic AIA 171 Å (top row) and 94 Å (bottom row) images showing the propagation of an EUV wave associated with a flux rope eruption in the simulation. The pink, blue, yellow, and green arrows indicate features that are described in Section 3.1. The three red arrows in (b) and (e) refer to the slits used to trace the propagation of the wave front. The animated version covers a time period from 12.1 to 743.7 s in the simulation.

(An animation of this figure is available.)

squared (n_e^2), which corresponds to the total emission measure spanning all temperatures.

Figure 3 presents the wave front in the 3D space and magnetic field lines that outline the flux rope. The perspective of Figure 3(c) roughly corresponds to the side view through the y -axis. A panoramic view that includes a temporal evolution is shown by the animation associated with this figure. As we can see in the animation, in the early stage of evolution, the shape of the wave front generally follows the shape of the flux rope, which indicates the key role of the flux rope eruption in driving the wave. In the later stage of evolution when the wave front has been detached from the flux rope, it becomes a dome-like and highly anisotropic structure in the 3D space that appears to be very different from EUV waves in previous 3D simulations (e.g., Cohen et al. 2009; Downs et al. 2012; Mei et al. 2020). The highly inhomogeneous wave front is given rise by the compression of plasma in coronal magnetic field above the complex active regions in this simulation (as shown in the gray-scale images in Figure 3). A recent multiperspective observation of coronal EUV wave by Feng et al. (2020) also found the inhomogeneity in the reconstructed wave front.

The quasi-periodic wave trains are not visible in the 3D view of the wave event. This may be because full 3D snapshots of the simulation are stored at a cadence of 2000 iterations that is 10 times lower than that for the synthetic AIA images. The background corona is very dynamic and undergoes rapid changes during the flare. Therefore, the low-amplitude quasi-periodic wave trains are more likely to be contaminated by the changes of the background corona, when taking a running difference with the low-cadence data. By comparison, the line-of-sight superimposition of the synthetic 2D AIA images can help to improve the signal-to-noise ratio of the wave trains. However, in the 3D space it becomes more challenging to identify the wave trains. It would be intriguing to investigate

the behavior of the quasi-periodic wave trains in the 3D space, which will be carried out in a following project with a rerun of the simulation to output 3D data with a sufficiently high cadence.

3.2. Kinematics of the Coronal EUV Wave

To study the kinematics of the leading wave front, we select three different points at the wave front in the running difference of the synthetic AIA 171 Å image at $t = 281.4$ s. At each point, we draw a slit normal to the tangent of the wave front, which represents the propagation direction of the wave front (see the three red arrows in Figures 2(b) and (e)). Because the wave front remains in a relatively symmetric shape during the propagation, which implies that the kinematics on both sides of the apex are similar, we place all three slits on the left side of the apex for a higher contrast.

We extract along the three slits the intensity of AIA 171 Å running difference images from a time series of 100 snapshots (with a cadence of 13 s before and after the flare and 2.2 s in the impulsive phase). This yields the time–distance diagrams shown in the top row of Figure 4. We can discern many short ridges in low contrast near the head of each slit between $t = 160$ and 200 s, and some of them could reach much longer distances in the diagram. These correspond to the small ripples triggered by the flux rope eruption during the impulsive phase of the flare as we have seen in Figure 2. However, their low contrast means that it would be almost impossible to identify them in real observations.

The *observable* leading wave front can be clearly identified in the time–distance diagrams as a long and narrow ridge that is significantly brighter than the surroundings. For each slit, we first extract the positions of the wave front, as marked by the red crosses in the top row of Figure 4. Then, we perform a

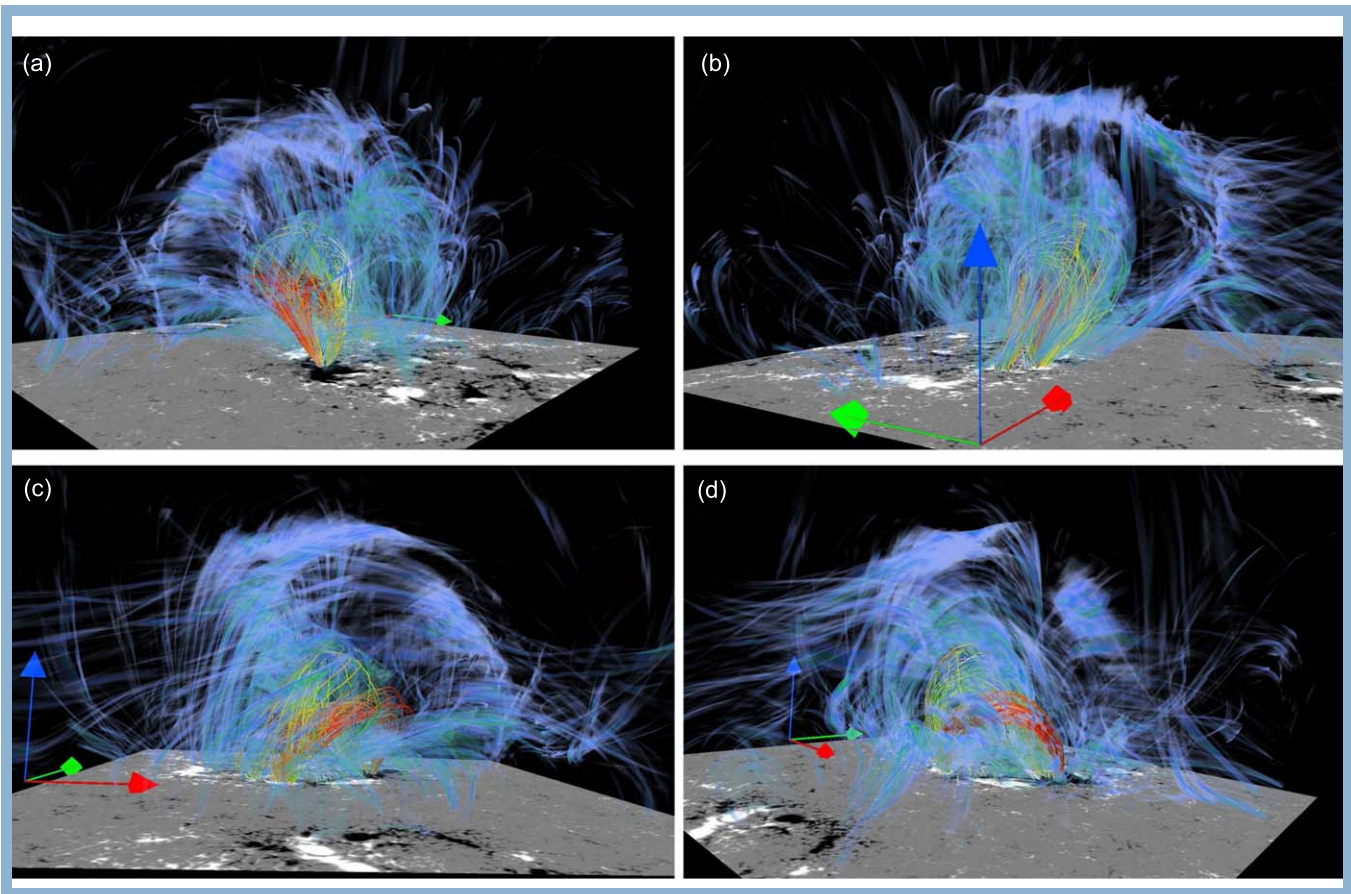


Figure 3. The wave front in the 3D space. This snapshot is at $t = 281$ s, which is the same as that for Figure 2. The red, green, and blue arrows identify the origin of the Cartesian coordinate system in the simulation. The data have been shifted in the y -direction (periodic), such that the eruption is placed in the center region of the domain. The blue-colored structure shows the wave front by the running difference of n_e^2 . The magnetic field lines represent the rising magnetic flux rope, and their color indicates the temperature of plasma there, with white for cool plasma (10^5 K) and red for hot plasma (10^7 K). The 3D visualization is produced by VAPOR (Clyne et al. 2007). The animated version shows the wave front from multiple perspectives.

(An animation of this figure is available.)

cubic Lagrangian interpolation on the curve of the positions (as a function of time), and the derivative of this curve yields the propagation speed of the wave front.

The derived speeds along the three slits are plotted as black crosses in Figures 4 (d), (e), and (f), respectively. The blue lines show linear fittings to the propagation speeds. In each direction, the EUV wave decelerates at a roughly constant rate when it propagates farther away from the source region. The deceleration can also be clearly seen in the time–distance diagrams shown in the top row of Figure 4, as the slope of the wave front gradually decreases. When comparing the results among the different slits, we find that the flank of the wave front (slit 3) has a higher propagation speed in the early stage and a larger deceleration rate afterward than the apex.

3.3. The Shock Nature of the Coronal EUV Wave

It is straightforward to clarify in this simulation whether the wave front is sub- or super-Alfvénic, which is also an important question for EUV waves observed on the real Sun. We calculate the speed of fast magnetoacoustic waves (v_f) in the simulation domain and plot v_f at the location the wave front passes in the bottom row of Figure 4. During the early propagation (i.e., before $t = 280$ s), the EUV wave in our

simulation is clearly a shock with an average Mach number (in relative to v_f) of about 1.2. However, as the wave travels farther, it gradually degenerates into a fast magnetoacoustic wave.

We further check the changes of plasma properties and magnetic field across the wave front. For this purpose, we cut through the apex of the dome-shaped wave front in the 3D space with a vertical slab that is parallel to the x – z plane and has an extent of 10 pixels in the y -direction. Then we average the physical quantities over the y -direction of the slab, which yields a 2D slice.

We synthesize AIA 171 Å images for this 2D slice and display their running difference at $t = 281.4$ s in Figure 5(a). The wave front can be clearly identified, and the interface edge (i.e., the shock front) seen in this vertical cut appears to be much sharper than that shown in Figure 2(b), which suffers from the integration along the line of sight. The red arrow indicates the normal direction of the wave front (shock) and marks a segment of 9.7 Mm. We plot in Figures 5(b)–(e) the changes of plasma properties and magnetic field along this arrow, with the downstream (shocked medium) on the left of the shock front and upstream (undisturbed medium) on the right. The running difference of AIA images along the arrow is

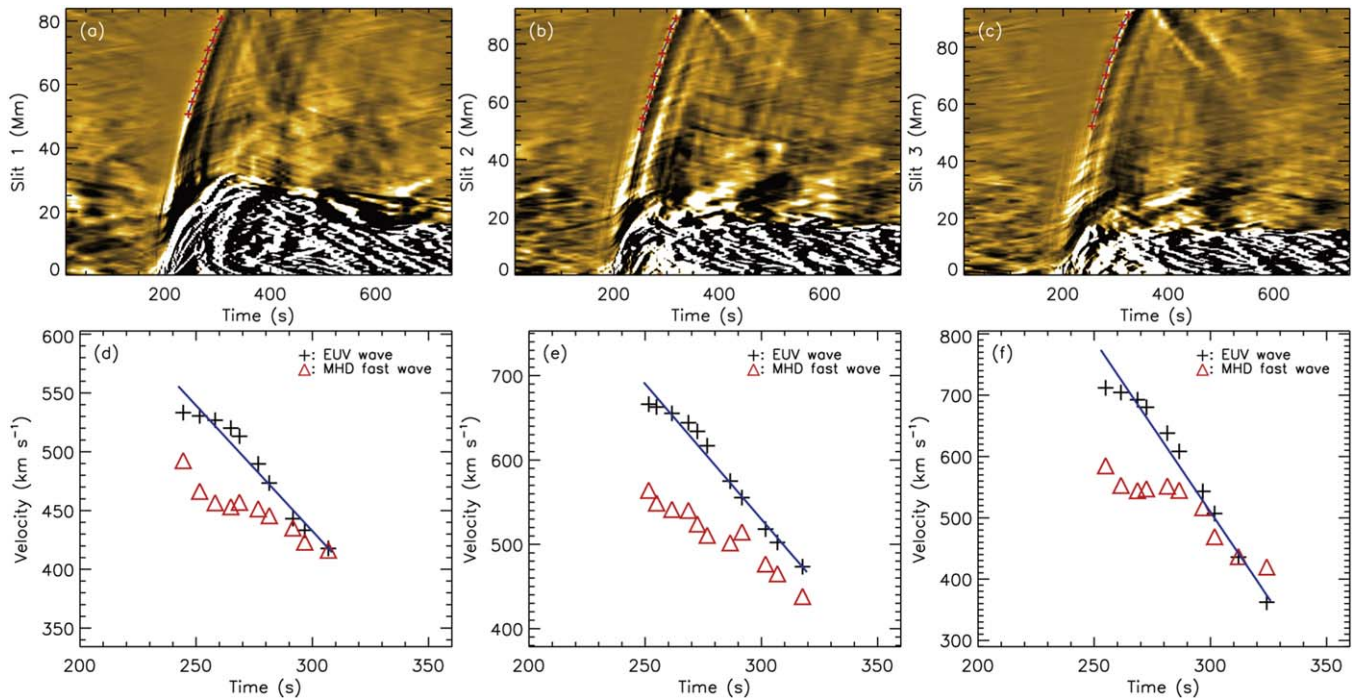


Figure 4. Time–distance diagrams and the propagation speeds of the wave front measured along the three slits. The left, middle, and right columns are for slits 1, 2, and 3, respectively. The horizontal axis represents the real physical time. The positions of the wave front are marked with red crosses in the top row. The black crosses in the bottom row show the propagation speed of the wave front as a function of time, while the red triangles show the local fast magnetoacoustic wave speed. The blue lines show linear fittings of the speed of the wave front.

also plotted in these four panels to mark the exact position of the wave front.

At the wave front the plasma density (Figure 5(b)) is increased³ by a factor of 1.2. The pressure (Figure 5(c)), which also represents the internal energy of the plasma, shows a similar behavior along the arrow and jumps for almost the same factor at the wave front. This implies that the temperature does not significantly change across the wave front. It is because the temperature is affected by many physical processes in the corona, and in particular the thermal conduction.

We present the change of magnetic field strength in Figure 5(d). The change of the direction of the magnetic field is illustrated by the angle (θ) between the magnetic vector and the normal vector of the wave front, as shown in Figure 5(e). There is an abrupt enhancement of the magnetic field strength at the wave front. Meanwhile, the angle also increases accordingly, which means that the tangential component of the magnetic field becomes stronger after the EUV wave has passed by. All the above variations of physical quantities indicate that the leading wave front is a fast-mode shock.

4. Discussion and Conclusion

4.1. Summary of Results

To explore the physical nature of EUV waves, we have analyzed an EUV wave event that occurs during a flare in a comprehensive RMHD simulation of the formation of solar active region through magnetic flux emergence. The EUV wave can be clearly identified from the running difference of synthetic AIA images, as was commonly detected in real observations. The main results are summarized as follows.

1. The first signature of the wave is many small ripples that are triggered by the lift of the magnetic flux rope during the impulsive phase of the flare. The most prominent wave front that would be considered as the leading wave front appears about only 50 s later and propagates through the entire domain in a semicircular shape.
2. We find quasi-periodic wave trains from both synthetic AIA images (Figure 2) and time–distance diagrams (Figure 4). They can be seen as secondary wavefronts behind the leading wave front and ahead of the front edge of the erupting flux rope, and exhibit a period of about 30 s.
3. The leading wave front is a fast-mode shock with an initial Mach number (relative to a fast magnetoacoustic wave) of about 1.2. The leading wave front gradually decelerates to a speed that is similar to the local fast magnetoacoustic wave.
4. The abrupt increases of the plasma density, pressure, and tangential magnetic field at the sharp wave front are well resolved and consolidate the (fast-mode) shock nature of the leading wave front. The change of physical parameters across the wave front provides a quantitative diagnostic on wave-affected coronal plasma.

4.2. Large-scale EUV Wave Driven by a Confined Eruption

The EUV wave in our simulation is clearly a piston-driven MHD shock, which is one of the earliest proposed interpretations (Warmuth 2015, and references therein). Moreover, the wave front is an integral component of the complex dynamics driven by the eruption of the flux rope, which has also been extensively studied in numerical simulations (e.g., Chen et al. 2002, 2005; Cohen et al. 2009; Downs et al. 2012; Xie et al. 2019; Mei et al. 2020).

³ Viewed from the upstream to the downstream (from the right to the left of the plot).

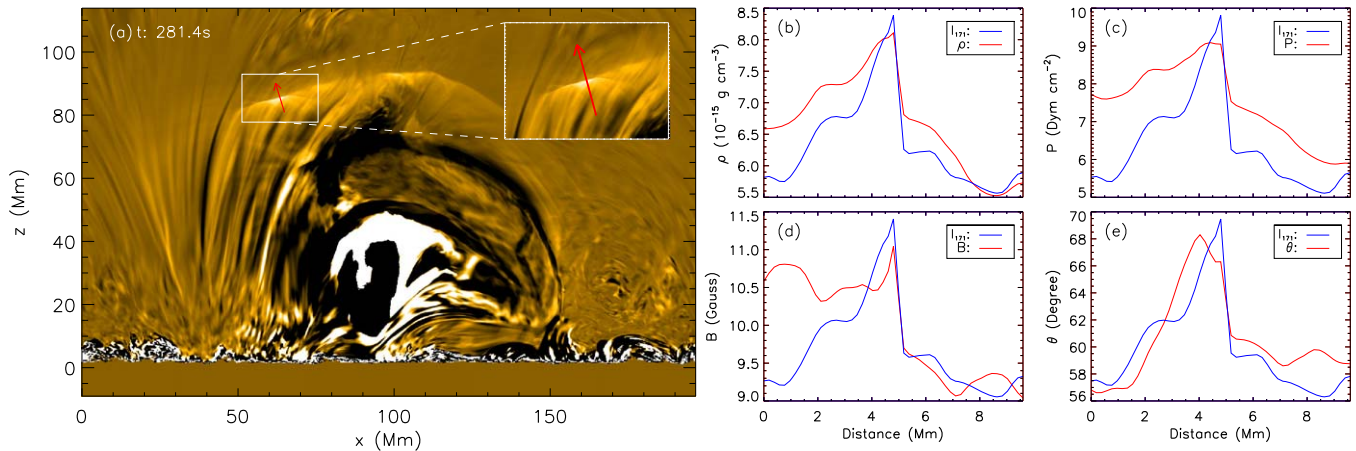


Figure 5. Changes of physical quantities across the wave front. (a) Running difference of synthetic 171 Å image for a 2D vertical slice cutting through the apex of the wave front. The red arrow indicates the normal direction of the wave front, a slit along which the physical quantities are displayed in (b)–(e). Variations of the plasma density (b), pressure (c), magnetic field strength (d), and the angle between the magnetic field and the normal direction of the wave front (e) along the arrow, with the smaller distance on the downstream and larger distance on the upstream. The wave front is at about 5.5 Mm. The blue lines in (b)–(e) are identical and plot the AIA 171 Å intensity. It is important to note that all the curves show the original physical quantities but not their running differences.

A unique feature of the event we study is that the eruption of the flux rope fails to become a coronal mass ejection (CME). Nevertheless, a large-scale shock/wave is generated by this eruption, and it clearly has a potential to propagate much farther if not limited by the size of the simulation domain. In observations, EUV waves are found to be closely related with CMEs (Cliver et al. 2005; Chen 2006). The event we study suggests that confined eruption can drive large-scale waves, as long as sufficient energy is released to the wave, and this can help to understand EUV waves observed in flares without CMEs.

In the unified picture of the EUV waves, in addition to the shock/wave component that can be generated by one strong piston push, a nonwave component is given rise by compression of the plasma outside the leading edge of the expanding CME (see, e.g., Chen et al. 2005; Cohen et al. 2009; Downs et al. 2012). The nonwave component is absent in the event analyzed in this study. The primary reason is that the flux rope stops rising at the height of about 50 Mm, and does not provide a persistent push that can compress the plasma in front of the flux rope.

4.3. Quasi-periodic Wave Trains

More detailed features of EUV waves revealed by recent observations pose new challenges to numerical models. Our simulation self-consistently reproduces quasi-periodic wave trains within a large-scale EUV wave, as found in the AIA observations (e.g., Liu et al. 2012; Yuan et al. 2013; Nisticò et al. 2014; Zheng et al. 2018; Shen et al. 2019).

Previously numerical simulations of the quasi-periodic wave trains usually employed idealized magnetic configurations and/or artificial triggers (e.g., Ofman et al. 2011; Pascoe et al. 2013; Takasao & Shibata 2016). On the other hand, large-scale simulations that consider a more realistic setup and coronal physics (Cohen et al. 2009; Downs et al. 2012) were not done with a sufficient spatial resolution to resolve the quasi-periodic wave trains. The simulation we presented in this Letter reproduces quasi-periodic wave trains as a component of a large-scale coronal EUV wave that spontaneously occurs in a complex and solar-like active region.

The event in our simulation resembles the general scenario proposed by Liu et al. (2012), except for the structures inside the CME front. They both follow a process that the eruption of a flux rope (expansion of a CME) drives a leading wave front that decouples from the driver and multiple periodic wavefronts propagating within the leading wave front and ahead of the flux rope (CME).

The wave trains in our simulation exhibit a period of about 30 s, which is a few times smaller than those seen in large-scale events (e.g., 128 s reported by Liu et al. 2012 and 163 s reported by Shen et al. 2019), but is similar to the 45 s period observed by Miao et al. (2019). The periodicity is suggested to originate from the quasi-periodic pulsations in flares (McLaughlin et al. 2018). Therefore, we suspect that the difference in periodicity might be due to the significant difference between the spatial scales of the source region that powers these cyclic behaviors. In order to substantiate the essential cause of the periodicity, it is necessary to investigate the 3D data with a much higher time cadence and preferably with a higher spatial resolution, which would require at least a rerun of the simulation with high-cadence output (with improved resolution if resources would permit). This will be carried out in a following project.

To conclude, the RMHD simulation can reproduce a comprehensive process of a solar flare that simultaneously drives a large-scale coronal EUV wave and quasi-periodic wave trains. The coronal EUV wave is a fast-mode MHD shock that decays to a fast magnetoacoustic wave. The overall picture is in line with the scenario deduced from decades of theoretical and observational studies of this phenomenon. Last but not least, the high-resolution 3D RMHD simulation also indicates that many fine structures and features of coronal EUV wave in the 3D space have not been fully revealed by current remote-sensing observations.

The authors thank the anonymous referee for helpful suggestions that improve the clarity of this Letter. F.C. acknowledges the support of Advanced Study Program (ASP) postdoctoral fellow of NCAR. The authors would like to acknowledge high-performance computing support from Cheyenne (doi:10.5065/D6RX99HX) provided by NCAR's

Computational and Information Systems Laboratory, sponsored by the National Science Foundation. This work was also supported by NSFC under grant 11733003.

ORCID iDs

Can Wang  <https://orcid.org/0000-0002-6799-4340>

Feng Chen  <https://orcid.org/0000-0002-1963-5319>

Mingde Ding  <https://orcid.org/0000-0002-4978-4972>

References

- Asai, A., Ishii, T. T., Isobe, H., et al. 2012, *ApJL*, 745, L18
- Athay, R. G., & Moreton, G. E. 1961, *ApJ*, 133, 935
- Attrill, G. D. R., Harra, L. K., van Driel-Gesztelyi, L., & Démoulin, P. 2007, *ApJL*, 656, L101
- Chen, F., Rempel, M., & Fan, Y. 2017, *ApJ*, 846, 149
- Chen, P. F. 2006, *ApJL*, 641, L153
- Chen, P. F., Fang, C., & Shibata, K. 2005, *ApJ*, 622, 1202
- Chen, P. F., Wu, S. T., Shibata, K., & Fang, C. 2002, *ApJL*, 572, L99
- Chen, P. F., & Wu, Y. 2011, *ApJL*, 732, L20
- Cheung, M. C. M., Rempel, M., Chintzoglou, G., et al. 2019, *NatAs*, 3, 160
- Cliver, E. W., Laurenza, M., Storini, M., & Thompson, B. J. 2005, *ApJ*, 631, 604
- Clyne, J., Mininni, P., Norton, A., & Rast, M. 2007, *NJPh*, 9, 301
- Cohen, O., Attrill, G. D. R., Manchester, W. B., I., & Wills-Davey, M. J. 2009, *ApJ*, 705, 587
- Cunha-Silva, R. D., Selhorst, C. L., Fernandes, F. C. R., & Oliveira e Silva, A. J. 2018, *A&A*, 612, A100
- Delannée, C., Török, T., Aulanier, G., & Hochedez, J. F. 2008, *SoPh*, 247, 123
- Downs, C., Roussev, I. I., van der Holst, B., Lugaz, N., & Sokolov, I. V. 2012, *ApJ*, 750, 134
- Fan, Y., & Fang, F. 2014, *ApJ*, 789, 35
- Feng, L., Lu, L., Inhester, B., et al. 2020, *SoPh*, 295, 141
- Fulara, A., Chandra, R., Chen, P. F., et al. 2019, *SoPh*, 294, 56
- Gopalswamy, N., Yashiro, S., Temmer, M., et al. 2009, *ApJL*, 691, L123
- Klassen, A., Aurass, H., Mann, G., & Thompson, B. J. 2000, *A&AS*, 141, 357
- Liu, R., Liu, C., Xu, Y., et al. 2013, *ApJ*, 773, 166
- Liu, W., & Ofman, L. 2014, *SoPh*, 289, 3233
- Liu, W., Ofman, L., Nitta, N. V., et al. 2012, *ApJ*, 753, 52
- Liu, W., Title, A. M., Zhao, J., et al. 2011, *ApJL*, 736, L13
- Long, D. M., Bloomfield, D. S., Chen, P. F., et al. 2017, *SoPh*, 292, 7
- McLaughlin, J. A., Nakariakov, V. M., Dominique, M., Jelínek, P., & Takasao, S. 2018, *SSRv*, 214, 45
- Mei, Z. X., Keppens, R., Cai, Q. W., et al. 2020, *MNRAS*, 493, 4816
- Miao, Y. H., Liu, Y., Shen, Y. D., et al. 2019, *ApJL*, 871, L2
- Moreton, G. E. 1960, *AJ*, 65, 494
- Muhr, N., Veronig, A. M., Kienreich, I. W., et al. 2014, *SoPh*, 289, 4563
- Nisticò, G., Pascoe, D. J., & Nakariakov, V. M. 2014, *A&A*, 569, A12
- Ofman, L., Liu, W., Title, A., & Aschwanden, M. 2011, *ApJL*, 740, L33
- Olmedo, O., Vourlidas, A., Zhang, J., & Cheng, X. 2012, *ApJ*, 756, 143
- Pascoe, D. J., Nakariakov, V. M., & Kupriyanova, E. G. 2013, *A&A*, 560, A97
- Rempel, M. 2017, *ApJ*, 834, 10
- Robbrecht, E., Verwichte, E., Berghmans, D., et al. 2001, *A&A*, 370, 591
- Shen, Y., Chen, P. F., Liu, Y. D., et al. 2019, *ApJ*, 873, 22
- Shen, Y., Liu, Y., Su, J., et al. 2013, *ApJL*, 773, L33
- Takasao, S., & Shibata, K. 2016, *ApJ*, 823, 150
- Thompson, B. J., Plunkett, S. P., Gurman, J. B., et al. 1998, *GeoRL*, 25, 2465
- Uchida, Y. 1974, *SoPh*, 39, 431
- Vögler, A., Shelyag, S., Schüssler, M., et al. 2005, *A&A*, 429, 335
- Warmuth, A. 2015, *LRSP*, 12, 3
- Warmuth, A., Vršnak, B., Magdalenic, J., Hanslmeier, A., & Otruba, W. 2004, *A&A*, 418, 1101
- Wills-Davey, M. J., DeForest, C. E., & Stenflo, J. O. 2007, *ApJ*, 664, 556
- Xie, X., Mei, Z., Huang, M., et al. 2019, *MNRAS*, 490, 2918
- Yuan, D., Shen, Y., Liu, Y., et al. 2013, *A&A*, 554, A144
- Zheng, R., Chen, Y., Feng, S., Wang, B., & Song, H. 2018, *ApJL*, 858, L1